

High frequency resonant response of a monopile in irregular deep water waves

Bjørn Hervold Riise^{1,2†}, John Grue¹, Atle Jensen¹ and Thomas Berge Johannessen²

¹Department of Mathematics, University of Oslo, Oslo, Norway

²DNV GL, Oslo, Norway

(Received xx; revised xx; accepted xx)

Experiments with a weakly damped monopile, either fixed or free to oscillate, exposed to irregular waves in deep water, obtain the wave-exciting moment and motion response. The nonlinearity and peak wave number cover the ranges: $\epsilon_P \sim 0.10 - 0.14$ and $k_P r \sim 0.09 - 0.14$ where $\epsilon_P = H_S k_P$ is an estimate of the spectral wave slope, H_S the significant wave height, k_P the peak wave number and r the cylinder radius. The response and its statistics, expressed in terms of the exceedance probability, are discussed as function of the resonance frequency, ω_0 in the range $\omega_0 \sim 3 - 5$ times the spectral peak frequency, ω_P . For small wave slope, long waves and $\omega_0/\omega_P = 3$, the nonlinear response deviates only very little from its linear counterpart. However, the nonlinearity becomes important for increasing wave slope, wave number and resonance frequency ratio. The extreme response events are found in a region where the Keulegan-Carpenter number exceeds $KC > 5$, indicating the importance of possible flow separation effects. A similar region is also covered by a Froude number exceeding $Fr > 0.4$ pointing to surface gravity wave effects at the scale of the cylinder diameter. Regarding contributions to the higher harmonic forces, different wave load mechanisms are identified, including: i) wave-exciting inertia forces, a function of the fluid acceleration; ii) wave slamming due to both non-breaking and breaking wave events; iii) a secondary load cycle; and iv) possible drag forces, a function of the fluid velocity. Also, history effects due to the inertia of the moving pile, are contributing to the large response events. The ensemble means of the 3rd, 4th and 5th harmonic wave-exciting force components extracted from the irregular wave results are compared to the FNV-theory (3rd harmonic) as well as other available experiments and calculations. The present irregular wave measurements generalize results obtained in deep water regular waves.

1. Introduction

In the offshore industry, there is a growing focus on lower cost and higher efficiency. This requires improved accuracy of the design conditions and enhanced optimized solutions (Zhen *et al.* 2015). A widely used offshore structure is the monopile. This is relevant for both the oil and gas business as well as to the renewable industry. In the development of new wind farms, the cylindrical structure has become a standard foundation type for the bottom fixed wind turbines. Typically the diameter is less than 8 m, the first natural period is 3-5 s and the damping is 1-4% of critical damping (Kallehave *et al.* 2015). In harsh wave environment these structures may be prone to high frequency resonant responses well above the governing wave frequency (Bredmose *et al.* 2013).

Regarding the high frequency responses, one distinguishes between *springing* and

† Email address for correspondence: bjorn.riise@gmail.com

ringing behaviour (Faltinsen 1993, p. 5). The *springing* motion is characterized by stationary oscillations, mostly caused by weakly nonlinear forces at the second harmonic of the governing wave frequency. The transient *ringing* response is characterized by a short build-up in time, typically within a wave period, and a longer decay time. The nonlinear loads causing *ringing* occur in steep waves, where large inertia forces are present. High or low pressure zones due to strong orbital velocities and possible flow separation effects may also contribute to the higher order forces (Grue *et al.* 1993; Paulsen *et al.* 2014b; Kristiansen & Faltinsen 2017). Wave slamming, due to steep and breaking waves, can lead to impulsive excitation, i.e. high frequency response with no build-up (Bredmose *et al.* 2013; Schl er *et al.* 2016).

Theories of the high frequency wave loads and ringing response in the realistic ocean environment still have shortcomings. Loading mechanisms, particularly in the strong waves, are not fully understood. Nor is the probability of the occurrence of an extreme response event clarified. Remaining challenges include development of methods which are sufficiently accurate in terms of the hydrodynamic loading. At the same time the short- and long term statistical variability of the wave conditions should be accounted for.

The hydrodynamic loads and responses, taking into account the short term variability of the wave conditions, are the focuses of present work. The long term variability, on the other hand, is not discussed. We note that, regarding the predictions of the long term variability, a complete long term analysis is required. However, to predict the response with a prescribed level of probability alternatives are *the environmental contour line method* (Haver & Winterstein 2009) or the use of a design wave, such as the *NewWave model* (Tromans *et al.* 1991). To ensure that the predicted response level is correct, it is vital that the waves driving the extreme response events and the significant loading mechanisms are both included in the analysis.

1.1. Previous work

Several model tests with monopiles have been carried out investigating the load mechanisms that excite the high frequency *ringing* response. Grue *et al.* (1993), Grue *et al.* (1994) and Chaplin *et al.* (1997) studied the force in focusing waves, Huseby & Grue (2000) in regular waves, and Grue & Huseby (2002) in the transient part of a regular wave train, while Stansberg *et al.* (1995), Marthinsen *et al.* (1996), Stansberg (1997) and Bredmose *et al.* (2013) discussed the *ringing* response in irregular waves.

The findings from the previous model tests point to nonlinear inertia loading in steep waves, generating high frequency transient force oscillations around 3 to 4 times the governing wave frequency. While the first harmonic force is well defined, the higher harmonic forces deviate from the predictions, particularly for increasing wave slope. Irrespective of which load mechanisms that exist, the high frequency response occurs due to significant nonlinearities. There are three possible sources for these nonlinearities as listed by Tromans *et al.* (2006): the wave motion, the hydrodynamic loading and the dynamic response of the structure itself.

The industry has traditionally obtained the wave loads by the *Morison's formula* (Morison *et al.* 1950) with an empirical adjustment of the wave kinematics such as the *Wheeler stretching* incorporated (Wheeler 1970). As the inertia term in Morison's formula only includes the force to a first approximation, disregarding possible significant nonlinear contributions (Lighthill 1979, 1986), a number of theoretical works have addressed the issue of the high frequency nonlinear loading. Linear and second order diffraction solutions capture the first and second harmonic forces in regular and irregular waves, while the solution obtained by Malenica & Molin (1995) capture the third harmonic force in regular waves. A long wave approximation (with $kr < 0.14$, k the

wave number, r the cylinder radius, see figure 7) developed by Faltinsen, Newman and Vinje (Faltinsen *et al.* 1995), referred to as FNV, was first obtained for regular waves, and secondly generalized by Newman (1996) to the case of irregular waves. Later Krokstad *et al.* (1998) proposed a modification to the FNV method, where the linear and second order contributions were replaced by the complete diffraction solutions. The method was combined with the third order contribution from the long wave approximation. With an appropriate description of the wave kinematics for realistic wave spectra, Johannessen (2010, 2012) obtained good agreement between the modified FNV method and measurements of a monopile exposed to irregular deep water waves .

An alternative nonlinear load description, based on energy consideration, was obtained by Rainey (1989, 1995*a,b*). The benefit of the Rainey method is that it takes undisturbed wave kinematics as input. This allows for both nonlinear wave motion and short-crestedness to be taken into account. This is in contrast to the FNV method, which is based on the underlying linear wave assumption in an unidirectional sea.

Computational Fluid Dynamics (CFD) is increasingly being used to calculate the wave loads on offshore structures, see Paulsen *et al.* (2014*a*) and Paulsen *et al.* (2014*b*). Although CFD is capable of capturing the nonlinearities, the downside is that it is resource demanding. This adds restrictions to the length of the analyses with an irregular wave input. Recently, the FNV method has been generalized to a finite water depth by Kristiansen & Faltinsen (2017).

1.2. Focuses of present work

We here investigate the high frequency resonant response of a monopile exposed to irregular waves in deep water, where the short term statistical variability of the wave conditions is accounted for. The following subjects are included:

i) We carry out a set of laboratory experiments with a single bottom hinged, rigid cylinder in two different set-ups (§2). In the first set-up the cylinder is fixed. The response of an oscillating cylinder is then calculated from the measured wave-exciting moment. The cylinder in the second set-up is free to oscillate where the motion response is measured (§3.1).

ii) In the single wave events of the irregular waves, we identify local proxies such as the local trough-to-trough period and crest height. The higher harmonic load contributions are then investigated, obtaining the third, fourth and fifth harmonic load components in the irregular waves, comparing to published results in regular waves (FNV, Huseby & Grue (2000), Paulsen *et al.* (2014*b*)) (§3.2).

iii) We identify and investigate several different wave load mechanisms that are present during the large response events (§3.3).

iv) While previous investigations have typically focused on the wave loads acting on the structure only, the present work obtains both the force and the resulting motion. We present the response as function of resonance frequency which is varied in the range 3-5 times the peak wave frequency. We obtain the short term exceedance probability of the response maxima. The linear and nonlinear contributions to the response statistics are compared (§3.4).

v) The most extreme response events are discussed in terms of the local wave slope and nondimensional trough-to-trough period (§3.5).

A conclusion is given in §4.

Series	H_S [cm]	T_P [s]	$T_P\sqrt{g/d}$	k_{Pr}	$k_P h$	ϵ_P	ω_0/ω_P
a	6.45	1.157	14.8	0.09	2.22	0.10	3.3
b	7.73	1.156	14.8	0.09	2.22	0.12	3.3
c	6.24	1.044	13.4	0.11	2.68	0.12	2.9
d	5.20	0.939	12.0	0.14	3.30	0.12	2.6
e	9.01	1.157	14.8	0.09	2.22	0.14	3.3
f	6.12	0.939	12.0	0.14	3.30	0.14	2.6

TABLE 1. Sea state parameters. Significant wave height H_S , peak wave period T_P , normalized peak wave period $T_P\sqrt{g/d}$, normalized wave number k_{Pr} , normalized water depth $k_P h$, spectral wave slope $\epsilon_P = 0.5H_S k_P$ and resonance frequency ratio ω_0/ω_P as obtained from the oscillating cylinder.

2. Experiments

2.1. Wave tank

The experiments were carried out in the wave flume in the Hydrodynamic Laboratory at the University of Oslo. The wave flume is 25 m long, 0.5 m wide and was filled to a water depth of $h = 0.72$ m. In one end of the tank there is a hydraulic piston-type wavemaker with motion controlled by a preset voltage time series based on linear wavemaker theory. In the opposite end there is a passive absorbing beach. At the location 10.9 m from the wavemaker, a bottom hinged cylinder, with a diameter $d = 6$ cm, was placed to obtain the wave-exciting moment and the motion response.

2.2. Wave conditions

A total of six irregular long-crested wave time series based on the JONSWAP spectrum (Hasselmann *et al.* 1973), each 320 seconds long, were used in the experiments. The JONSWAP spectrum was chosen to generate an approximately real ocean wave environment. The spectrum as a function of angular frequency ω is given by

$$S_J(\omega_n) = A_\gamma \alpha \omega_n^{-5} \exp\left(-\frac{5}{4}\omega_n\right)^{-4} \gamma^{\exp\left(-\frac{1}{2\sigma^2}(\omega_n-1)^2\right)}, \quad (2.1)$$

where $\omega_n = \omega/\omega_P$ and $\alpha = (5/16)\omega_P^{-1}H_S^2$. The peak wave frequency is denoted by $\omega_P = 2\pi/T_P$ and the significant wave height by $H_S = 4\sigma_\eta$, where T_P is the peak wave period and σ_η is the standard deviation of the measured surface elevation. The peak shape parameter is $\gamma = 3.3$, the spectral width parameter is $\sigma = 0.07$ for $\omega \leq \omega_P$ and $\sigma = 0.09$ for $\omega > \omega_P$. Further, $A_\gamma = 1 - 0.287 \ln(\gamma)$ is a normalization factor.

To relate the wave-exciting moment and motion response to undisturbed wave parameters, the surface elevation was measured with the cylinder removed, using ultra sound wave sensors (UltraLab ULS Advanced Ultrasound, USS02/HFP with 250 Hz sampling rate). The waves were measured at the location for the cylinder, in addition to 0.12 m and 4.9 m upstream, and 4.4 m downstream.

The governing wave parameters of the six time series, given by the H_S and T_P at the location for the cylinder, are listed in table 1. Here the peak wave number k_P is found from the linear dispersion relation $\omega_P^2 = gk_P \tanh(k_P h)$, where g is the acceleration of gravity and h is the water depth. The normalized water depth, $k_P h$, is in the range 2.2–3.3 which is considered as deep water waves, and the spectral wave slope, $\epsilon_P = 0.5H_S k_P$, is in the range 0.10–0.14 which is considered as moderately steep waves. The normalized wave number, k_{Pr} , where r is the radius of the cylinder, is in the range 0.09–0.14 which is

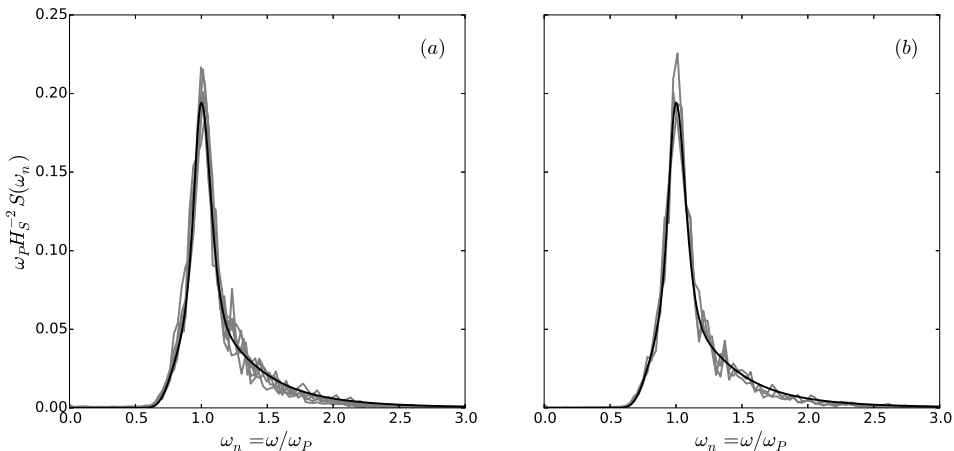


FIGURE 1. Wave energy density spectrum. Measured surface elevation and JONSWAP spectrum with $\gamma = 3.3$ for (a) all the six time series and (b) time series c, where $H_S = 6.24$ cm and $T_P = 1.044$ s, measured at the location for the cylinder, in addition to 4.9 m upstream and 4.4 m downstream.

considered as outside of the diffraction regime. The corresponding nondimensional peak wave period is $T_P \sqrt{g/d} \sim 12 - 15$ where $d = 2r$.

All the six measured wave spectra show good agreement with the JONSWAP spectrum, as seen in figure 1a. In figure 1b, the spectrum from series c is shown at the cylinder location in addition to 4.9 m upstream and 4.4 m downstream, showing only minor modification in the spectral shape. Between the upstream and downstream location, the rate of decrease in H_S is found to be, on average of the six time series, 0.01 per peak wave length $\lambda_P = 2\pi/k_P$. Measurements from the two wave sensors with a distance of 0.12 m have been used to estimate the reflection from the beach. For the governing wave frequencies, $0.9 < \omega/\omega_P < 1.5$, the reflection coefficient, in terms of the amplitude, as outlined by Goda & Suzuki (1976), is found to be less than 0.06.

2.3. Local wave properties and statistics

The surface elevation at a fixed position in the wave tank is a function of time. It is convenient to define a single wave event by its crest elevation, η_C , and its trough-to-trough period, T_{TT} , see figure 2a. All together, the six time series consist of totally 2166 single wave events. A scatter plot of η_C and T_{TT} , measured at location for the cylinder is shown in figure 2b.

The empirical probability of exceedance for the events is given by

$$P_{ex}(x_i) = 1 - P(X \leq x_i) = 1 - i/(N + 1), \quad (2.2)$$

where x_i for $i = 1, 2, \dots, N$ indicates the events in ascending order, and N is the total number of events. In figure 3a the exceedance probability $P_{ex}(\eta_C/H_S)$, as found from series c, is presented and compared to the linear Rayleigh and the second order Forristall crest distribution (Forristall 2000). It is observed that the measurements contain somewhat larger crest heights than expected based on the second order distribution. This is further visualized by comparing the largest crest elevations from all of the series with the corresponding Forristall distribution. If η_F denotes the Forristall crest height estimate, the largest crest height observed with regards to significant wave height, $\eta_C/H_S = 1.5$,

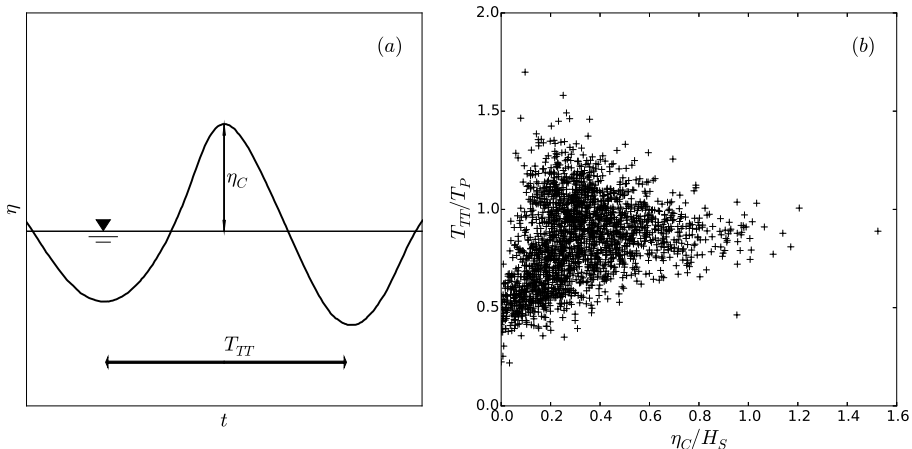


FIGURE 2. Local wave properties. (a) Definition of crest height η_C and trough-to-trough wave period T_{TT} of a wave event and (b) wave scatter plot including all the 2166 measured waves (+).

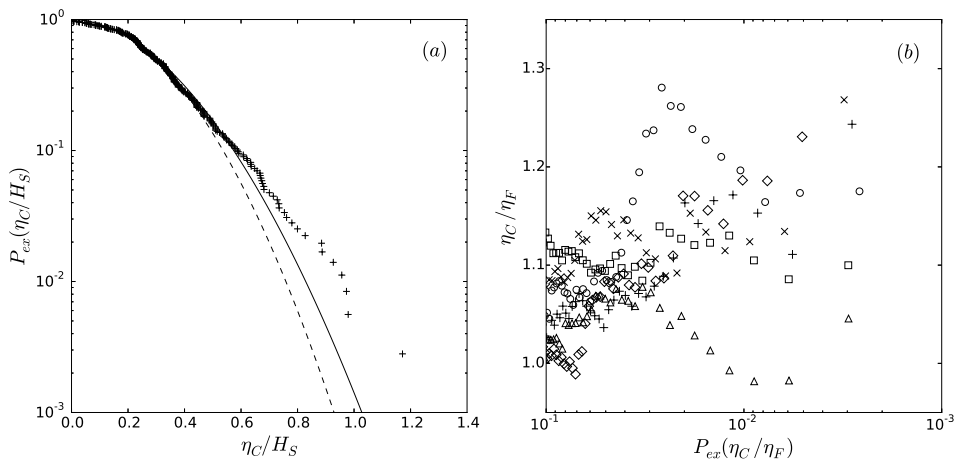


FIGURE 3. Crest height exceedance probability for (a) series c, $H_S = 6.24$ cm and $T_P = 1.044$ s (+), linear Rayleigh (—) and second order Forristall (—) and (b) measured crest heights, normalized with Forristall estimate, the 10% largest crest heights from each series, series a (Δ), b (\square), c (+), d (\diamond), e (\times) and f (\circ).

has $\eta_C/\eta_F = 1.6$ (found in series d and seen in figure 2). Except for this extreme crest event, a plot of η_C/η_F versus its probability shows $0.97 < \eta_C/\eta_F < 1.28$ for the 10% largest waves, for all of the six series, see figure 3b.

For later purposes (§3.2 and §3.5), following Grue *et al.* (2003), using a variant of the Stokes' third order approximation, the measured η_C and T_{TT} are used to define a local wave number, k_{TT} , and local wave slope, ϵ , of the event by

$$\omega_{TT}^2 = gk_{TT}(1 + \epsilon^2) \quad \text{and} \quad k_{TT}\eta_C = \epsilon + \frac{1}{2}\epsilon^2 + \frac{1}{2}\epsilon^3, \quad (2.3)$$

where $\omega_{TT} = 2\pi/T_{TT}$, $\epsilon = ak_{TT}$ and a is the approximated underlying linear amplitude.

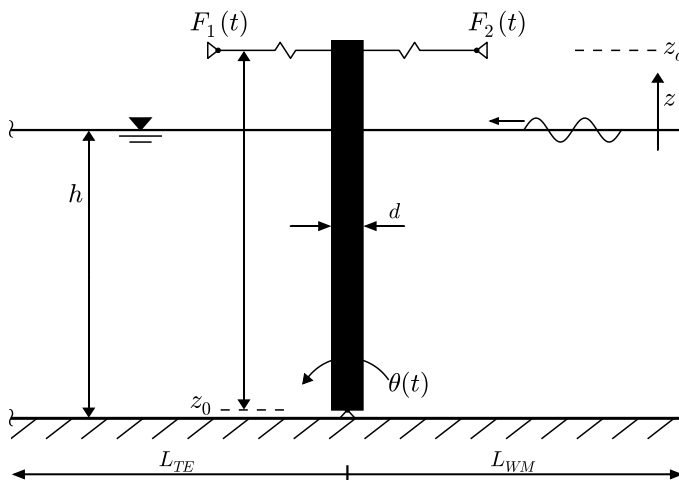


FIGURE 4. Oscillating cylinder set-up with angular rotation $\theta(t)$, cylinder diameter $D = 0.06$ m, water depth $h = 0.72$ m, rotation point $z_0 = 0.02$ m, distance from tank bottom to load cells $z_a = 0.92$ m, load cells F_1 and F_2 , distance to wavemaker $L_{WM} = 10.90$ m and distance to tank end, $L_{TE} = 13.87$ m .

This enables a wave parametrisation of each of the single wave events in the irregular wave time series. From the same approach a maximum horizontal particle velocity below the crest is estimated by $u_C = \epsilon \sqrt{g/k_{TT}} \exp(k_{TT} \eta_C)$. The estimation of ϵ , k_{TT} and u_C in irregular waves have been further tested by Stansberg *et al.* (2008) and Grue & Jensen (2012), showing good agreement with experimental results.

2.4. Cylinder model

A single cylinder with diameter $d = 6$ cm, in two different set-ups, was used in the experiments. The cylinder was located at a location of 10.9 m from the wavemaker and hinged at a horizontal lateral axis at the level of $z = z_0 = 2$ cm above the tank bottom, with positive rotation in the wave propagation direction. At a distance of $z_a - z_0 = 90$ cm above the rotation axis, the cylinder was connected to two load cells (Hottinger Baldwin Messtechnik Type Z6C2 with 10 kg = 2mV/V and 400 Hz sampling rate), measuring the force from which the overturning moment was determined. In the first set-up the cylinder was fixed, rigidly connected to the load cells, where the wave-exciting force and moment with respect to z_0 are measured. In the second set-up the cylinder was free to oscillate, where springs were used to connect the model and the load cells.

A sketch of the second set-up is shown in figure 4. The vertical cylinder is free to rotate with an angle $\theta(t)$ in the pitch mode of motion. Assuming linear motion, the moment due to the pressure forces with respect to z_0 reads: $M_{wave}(t) - a_{55}\dot{\theta} - b_{55}\dot{\theta} - c_{55}\theta$, where $M_{wave}(t)$, a_{55} , b_{55} and c_{55} denote the wave exciting moment obtained from the fixed cylinder set-up, added mass, damping and restoring coefficients in the pitch mode of motion, respectively. The moment due to the spring forces reads: $-(z_a - z_0)(F_2(t) - F_1(t)) = -\kappa_0(z_a - z_0)^2\theta$ where F_1 and F_2 denote the force recorded on the left and right

transducer, respectively, see figure 4, and κ_0 the spring constant. Balance of angular momentum gives

$$m_{55}\ddot{\theta} = -a_{55}\dot{\theta} - b_{55}\dot{\theta} - (\kappa_0(z_a - z_0)^2 + c_{55})\theta + M_{wave}(t), \quad (2.4)$$

where m_{55} denotes the moment of inertia of the cylinder.

The resonance frequency of (2.4) is given by $\omega_0^2 = (c_{55} + \kappa_0(z_a - z_0)^2)/(m_{55} + a_{55})$. Note that the spring force provides the dominant contribution to the restoring force where c_{55} is 0.005 times $\kappa_0(z_a - z_0)^2$ for the actual cylinder. The still water decay tests as well as the irregular wave experiments determine $\omega_0 = 17.7$ rad/s $\sim 3\omega_P$ (table 1) of the oscillating cylinder. The damping ratio ζ , determined as the fraction of the critical damping, is 0.02 for the cylinder. The small damping ratio implies a very lightly damped oscillating system relevant to offshore wind turbines in extreme conditions (Kallehave *et al.* 2015).

By integration, the pitch angle $\theta(t)$ is obtained as function of time. For convenience, the response is multiplied by $\kappa_0(z_a - z_0)^2$ obtaining the moment of the sum spring force with respect to z_0 . We denote this quantity by $R(\omega_0, t)$ where

$$R(\omega_0, t) = \kappa_0(z_a - z_0)^2\theta(t) = \frac{\omega_0^2}{\omega_d} \int_0^t M_{wave}(\tau) e^{-\zeta\omega_0(t-\tau)} \sin(\omega_d(t-\tau)) d\tau, \quad (2.5)$$

and $\omega_d = \omega_0\sqrt{1-\zeta^2}$. A derivation of (2.5), commonly known as the Duhamel's integral, is given in appendix A. Using (2.5) to obtain the motion response $R(\omega_0, t)$, this is fully described by the wave-exciting moment, the resonance frequency and the damping ratio. Use of (2.5) makes possible a response analysis given $M_{wave}(t)$ on the fixed cylinder varying the resonance frequency ω_0 to investigate the response dependency on the ratio ω_0/ω_P . We shall find a good correspondence between the measured and calculated response maxima, see §3.1

For the calculations of the response, a low pass filter has been applied above the significant wave frequencies at the frequency $\omega = 60$ rad/s $> 9\omega_P$. This is considered as well above the significant wave and load frequencies of interest.

3. Wave loads and responses

The surface elevation, wave-exciting moment and motion response for a large event, occurring between two subsequent zero up-crossings of the moment history, are shown in figure 5. The various plots in the figure illustrate different effects observed in the run; these different effects are discussed in §3.1, §3.2 and §3.3. The zero up-crossing period of the moment, $T_{z_0}^M$, is illustrated in figure 5b. The periods T_{TT} and $T_{z_0}^M$ occur approximately in the same time window, but they are not exactly equal. The period T_{TT} is used in combination with the measured wave elevation to define the wave proxies, ϵ and k_{TT} in eq. (2.3), for presentation of the higher harmonic forces in §3.2 and the extreme response events in §3.3 and §3.5. The $T_{z_0}^M$ is used in combination with the wave-exciting moment time series obtaining the load and response statistics, using (2.2), with results presented in §3.1 and §3.4.

The wave event occurs in time series c where $T_P = 1.044$ s and $\omega_P = 2\pi/T_P$, giving a frequency ratio of $\omega_0/\omega_P = 2.9$ where $\omega_0 = 17.7$ rad/s. The surface elevation in figure 5a is normalized by the significant wave height H_S , and the load and responses in figures 5b-5g are normalized by the standard deviation of the wave-exciting moment, σ_M . Three repetitions of the time series are included in the figure and we note that the repeatability is good with only very small differences at the wave crest.

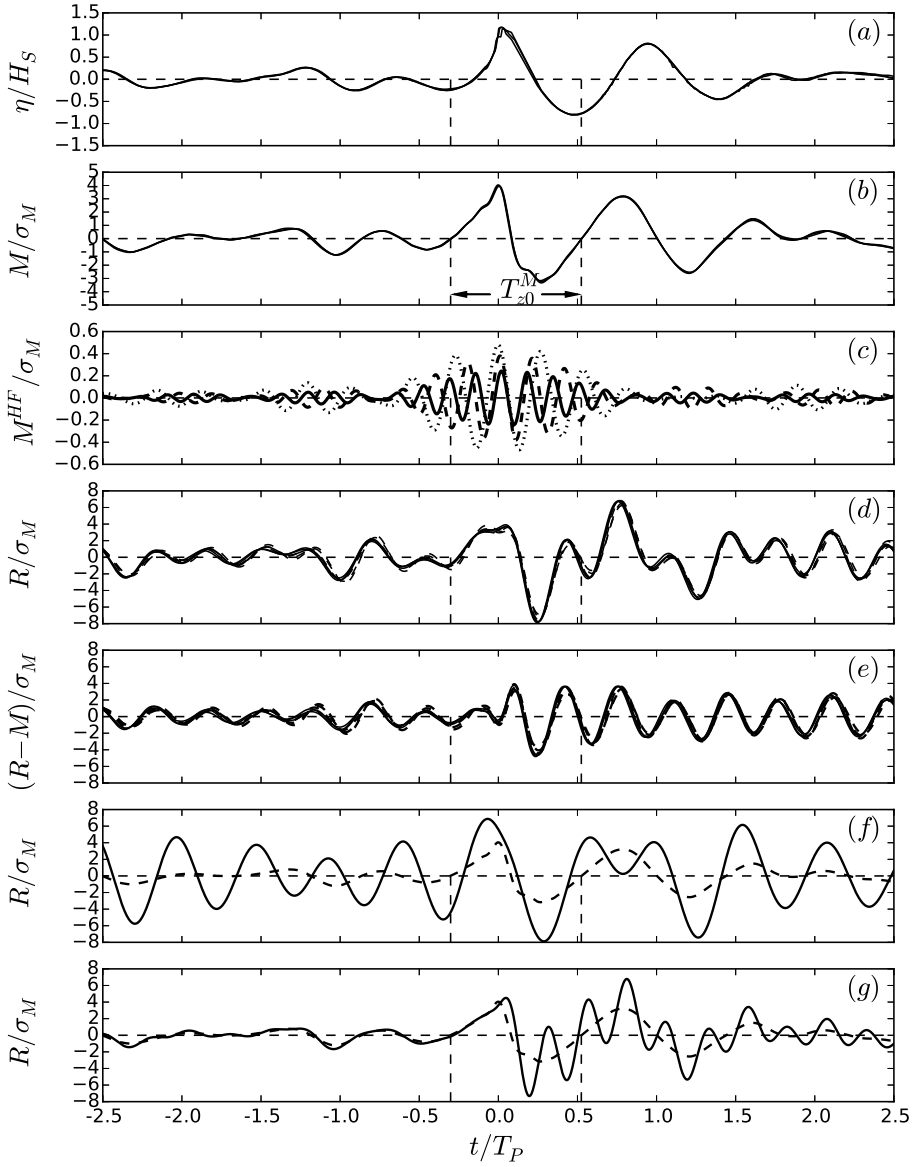


FIGURE 5. Series c ($t = 155.7$ s), $H_S = 6.24$ cm, $T_P = 1.044$ s. (a) Surface elevation, (b) wave-exciting moment, (c) higher harmonic wave force components, $(h - z_0)F^{(3\omega_{TP})}$ (\cdots), $(h - z_0)F^{(4\omega_{TP})}$ ($- -$), $(h - z_0)F^{(5\omega_{TP})}$ ($-$), (d) measured ($-$) and calculated ($- -$) response for $\omega_0/\omega_P = 2.9$, (e) measured ($-$) and calculated ($- -$) dynamic contribution for $\omega_0/\omega_P = 2.9$, (f) calculated response ($-$) and measured wave-exciting moment ($- -$) for $\omega_0/\omega_P = 2.0$ and (g) calculated response ($-$) and measured wave-exciting moment ($- -$) for $\omega_0/\omega_P = 4.0$.

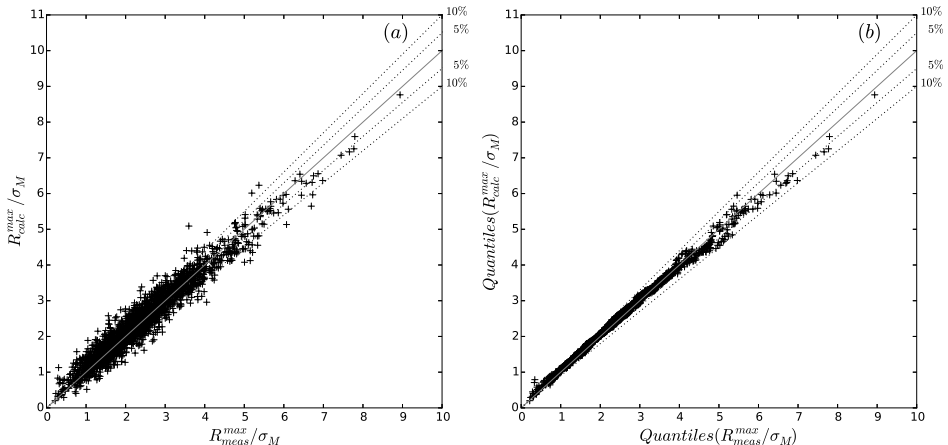


FIGURE 6. All of the six time series with 2166 events (+) where $2.6 < \omega_0/\omega_P < 3.3$. Comparing response maxima by (a) direct comparison and (b) quantiles (sorted values).

The different types of high frequency response may be categorized either as springing or ringing. In figure 5f and 5g calculations have been carried out for two different resonance frequencies, of $\omega_0/\omega_P = 2$ and $\omega_0/\omega_P = 4$, respectively, using the measured wave-exciting moment and the transfer function. The results illustrate a response of the springing type ($\omega_0/\omega_P = 2$) and of the ringing type ($\omega_0/\omega_P = 4$). The springing behaviour is global in time, while ringing is local in time.

3.1. Single response maxima

The response maxima, obtained from the measured wave-exciting moment on the fixed cylinder, with the resonance calculated by the transfer function eq. (2.5), denoted by $R_{calc}^{max} = \max(R(\omega_0, t))$, are compared to the measured response, denoted by R_{meas}^{max} . The data from all of the six time series give a total of 2166 events with a frequency ratio in the range $2.6 < \omega_0/\omega_P < 3.3$. The two quantities show good agreement for the largest response events, $R_{meas}^{max}/\sigma_M > 7$, where a deviation is up to approximately 5 %, see figure 6a. Good agreement is also found when looking at the calculated and measured maxima, sorted according to their magnitude, denoted by the so-called quantiles, see figure 6b. This justifies the use of the measured wave-exciting moment in combination with the transfer function, both for estimating the probability levels and for the identification of the extreme events. In what follows, we obtain only the calculated response maxima using the notation $R^{max} = R_{calc}^{max}$, for the extended frequency range $\omega_0/\omega_P = 3, 4$ and 5.

3.2. Higher harmonic wave forces

The high frequency response is driven by higher harmonic wave force components. We investigate the 3rd, 4th and 5th harmonic forces with regards to the local wave period T_{TT} . The forces are obtained from the wave-exciting moment assuming that they are acting at the still water level. The high frequency forces are considered to act close to the surface (Rainey 1989, 1995a,b; Faltinsen *et al.* 1995; Newman 1996), which indicates an error less than (η_C/h) when using the moment to obtain the forces. For each of the single events, where an event is defined in figures 5a and 5b, a window function of 20 s has been applied, from which the high frequency harmonic force components are extracted,

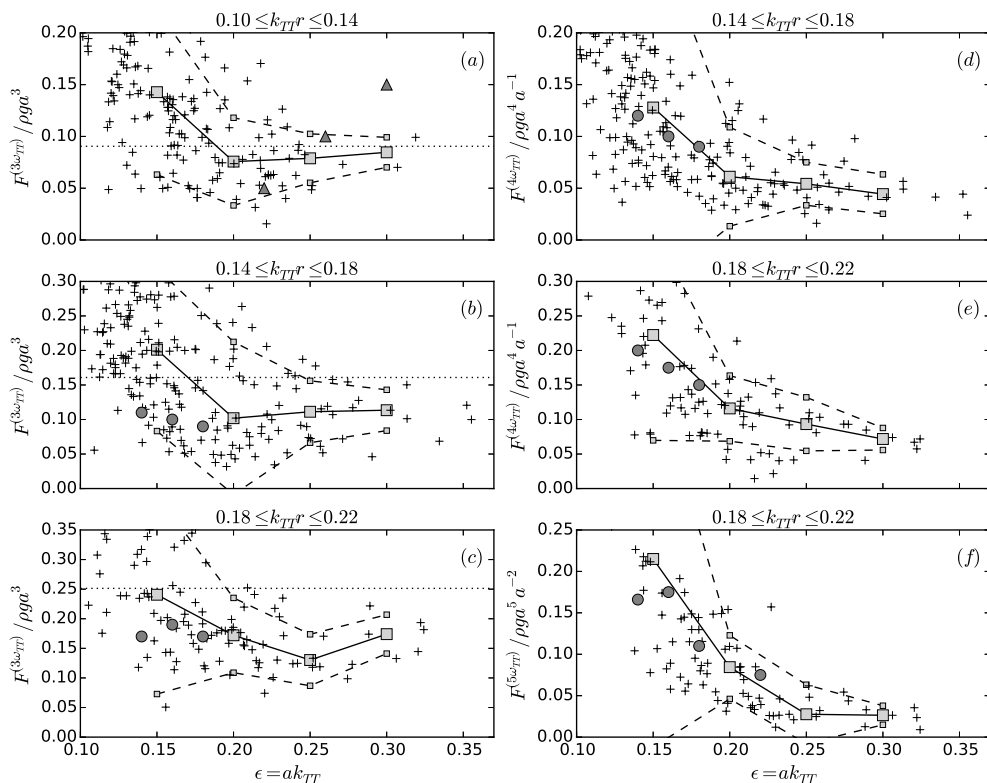


FIGURE 7. Higher harmonic wave force components. Individual events (+), ensemble average (—■) and standard deviation (---■), $F_{FNV}^{(3)}$ (···), H&G (●), and Paulsen *et al.* (2014b) for finite water depth (▲). (a) $F^{(3\omega_{TT})}$ for $0.10 \leq k_{TT}r \leq 0.14$, (b) $F^{(3\omega_{TT})}$ for $0.14 \leq k_{TT}r \leq 0.18$, (c) $F^{(3\omega_{TT})}$ for $0.18 \leq k_{TT}r \leq 0.22$, (d) $F^{(4\omega_{TT})}$ for $0.14 \leq k_{TT}r \leq 0.18$, (e) $F^{(4\omega_{TT})}$ for $0.18 \leq k_{TT}r \leq 0.22$, and (f) $F^{(5\omega_{TT})}$ for $0.18 \leq k_{TT}r \leq 0.22$.

see figure 5c. The maximum amplitude found within the event, is defined as the local high frequency harmonic force contribution.

The 3rd harmonic force $F^{(3\omega_{TT})}$ is found using a filter covering $2.5 < \omega/\omega_{TT} < 3.5$. Likewise, the 4th harmonic force $F^{(4\omega_{TT})}$ is found for $3.5 < \omega/\omega_{TT} < 4.5$, and the 5th harmonic force $F^{(5\omega_{TT})}$ using $4.5 < \omega/\omega_{TT} < 5.5$. The forces are expressed for the proxies; the normalized wave number $k_{TT}r$ and the wave slope $\epsilon = ak_{TT}$, where both are defined in (2.3) and r is the cylinder radius. The obtained results from the irregular waves are compared to previous works with a regular wave input; the leading-order third harmonic FNV solution, $F_{FNV}^{(3)}/\rho g a^3 = 2\pi(k_{TT}r)^2$, the measurements from Huseby & Grue (2000), denoted by H&G, and the CFD computations on finite depth by Paulsen *et al.* (2014b).

For the longest waves, with $0.10 \leq k_{TT}r \leq 0.14$ ($14.1 > T_{TT}^0 \sqrt{g/d} > 11.9$, where T_{TT}^0 is the linear estimate) we observe that $F^{(3\omega_{TT})}$ is tending towards a constant level close to the FNV result, with the average of the irregular results approximately 11% below the theory (figure 7a). The FNV force is evaluated for the middle value of $k_{TT}r$ in each of the

$k_{TT}r$	$F^{(3)}$	$F^{(4)}$	$F^{(5)}$
0.12 ± 0.02	0.08	0.03	0.01
0.16 ± 0.02	0.11	0.05	0.03
0.20 ± 0.02	0.13	0.09	0.03

TABLE 2. The ensemble average of the higher harmonic wave force components $F^{(3)} = F^{(3\omega_{TT})}/\rho g a^3$, $F^{(4)} = F^{(4\omega_{TT})}/\rho g a^4 a^{-1}$ and $F^{(5)} = F^{(5\omega_{TT})}/\rho g a^5 a^{-2}$ for local wave number $0.10 < k_{TT}a < 0.22$ and wave slope $\epsilon = ak_{TT} = 0.25$.

$k_{TT}r$ -ranges. In the range $0.14 \leq k_{TT}r \leq 0.18$ ($11.9 > T_{TT}^0 \sqrt{g/d} > 10.5$), the results from H&G are lower, but within the standard deviation of the present irregular wave results. The average of the irregular wave results are approximately 29% below the FNV theory, when the waves are steep (figure 7b). For the shorter waves, with $0.18 \leq k_{TT}r \leq 0.22$ ($10.5 > T^0 \sqrt{g/d} > 9.5$), the results from H&G are close to the irregular wave results, tending towards the same level, which is $\sim 44\%$ below the theory (figure 7c). Compared to the results on finite depth by Paulsen *et al.* (2014b) for $k_{TT}r = 0.1$, a deviation is observed. However, Kristiansen & Faltinsen (2017) points at a substantial difference between the forces in deep water and finite depth.

For the 4th harmonic force, $F^{(4\omega_{TT})}$, the results show good agreement with H&G (figures 7d and 7e). The results for the 5th harmonic force, $F^{(5\omega_{TT})}$, are similar to those of H&G for $k_{TT}r = 0.245$, where the present results are obtained for the wider range of $0.18 < k_{TT}r < 0.22$ (figure 7f). A comparison between the normalized forces for $\epsilon = 0.25$ is provided in table 2.

The present extracted higher harmonic force components in the irregular waves, for $0.1 < k_{TT}r < 0.22$ and $0.1 < \epsilon < 0.32$, provide a quite strong generalization of the higher harmonic forces measured by H&G in the regular waves with $0.1 < \epsilon < 0.24$. This in spite of the present results being obtained from the wave-exciting moment, assuming a moment arm equal to the still water level. We note that the present irregular wave results have a significant standard deviation not observed in the regular wave measurements.

As expected for the 3rd harmonic forces, the FNV approximation is found to best fit the longest waves ($0.1 < k_{TT}r < 0.14$). In general we observe that the force components are tending towards a constant level for the steep waves. The compliance with the previous results in periodic waves, indicates that the high frequency contribution originates from nonlinearities and not from shorter linear free waves, since regular waves do not contain energy from linear free waves. Moreover, it illustrates that the local wave slope and the wave number defined in (2.3) are useful proxies of the local wave events.

3.3. Wave load mechanisms

In this section we discuss the following different wave load mechanisms driving the response:

- i) wave-exciting inertia forces, a function of the fluid acceleration;
- ii) wave slamming, due to both non-breaking and breaking wave events;
- iii) the secondary load cycle; and
- iv) possible drag forces a function of the fluid velocity.

Consider the wave-exciting moment in figure 5b where the maximum occurs for $t/T_P = 0$. This is simultaneous to the maximum wave crest and means that the orbital velocity is approximately horizontal and at maximum. The force at this instant is associated with wave breaking, slamming and possible viscous drag forces (Paulsen *et al.* 2014b; Kristiansen & Faltinsen 2017) and are included in the categories ii) and iv) above.

Consider then the negative response maximum in figure 5d, of absolute value $R^{max} \approx 8\sigma_M$ occurring at $t/T_P \approx 0.25$. This is approximately at the same time as the wave elevation has a zero down-crossing, corresponding to a maximum horizontal particle acceleration at the surface. The acceleration is associated with an inertia force and is in accordance with category i). Returning to the load history in figure 5b, the secondary load cycle (Grue *et al.* 1993) occurs slightly before the time of the negative response extreme.

The dynamic part of the response, $R(t) - M(t)$, further highlights the effects of the different load mechanisms i)-iv). In figure 5e we observe that the large wave crest produces a significant change of the response amplitude and its phase for $t/T_P > 0$. Between the two local response peaks at $t/T_P \approx -0.1$ and $t/T_P \approx 0.1$ the dynamic part experiences a local oscillation of the duration of half of the resonance period. The modification of the response is due to a strongly nonlinear impulse type of loading, originating from the slamming event. As a result, the dynamic contribution attains a value of $R(t) - M(t) \approx 4\sigma_M$ at $t/T_P \approx 0.1$. The response is further increased to $R(t) - M(t) \approx 5\sigma_M$ around the wave zero down-crossing, at $t/T_P \approx 0.25$, with load contributions from the large inertia force and the secondary load cycle. Another effect that adds to the large negative response peak is the restoring force of the cylinder. Even with no wave-exciting forces, this would cause a negative response peak after the positive build-up. The timing of this, relative to the wave forces, is governed by ω_0 , the natural frequency. A result of the different load contributions working together, is that the maximum response occurs after and in the opposite direction of the maximum wave-exciting moment, approximately at the same time as the wave elevation has a zero down-crossing.

We have now discussed the load event in figure 5. Further, we consider the load histories of the 21 largest response events which are listed in table 3. More specifically, these events are obtained with regards to R^{max}/σ_M for $\omega_0/\omega_P = 3$. We observe that different wave load and response mechanisms contribute to the response level, including:

- a large nonlinear inertia force before the wave crest has passed, $F_{I,front}$, which is observed for 15 of the 21 events. The inertia force is characterized by the front of the wave being steep with $\Delta\eta/\Delta t > 5H_S/T_P$;
- a large nonlinear inertia force after the wave crest has passed, $F_{I,back}$, observed for 16 of 21 events. This is characterized by the back of the wave being steep with $\Delta\eta/\Delta t < -5H_S/T_P$;
- wave slamming, F_{slam} , observed for 8 of 21 events, including the 4 largest events. Here slamming is characterized by a coinciding wave crest and a maximum wave-exciting moment; and
- the secondary load cycle, F_{II} , observed for 17 of 21 events. The F_{II} s are found to coincide with a steep crest back and occur close to the wave zero down-crossing.

Further we note:

- an opposite direction of the maximum response, R_{opp} , characterized by the maximum response occurring after and in the opposite direction of the maximum wave-exciting moment and simultaneous to the wave zero down-crossing. This is observed for 16 of 21 events;
- an effect of a preceding wave, λ_{prec} , where the response is affected by the inertia of the moving pile. The oscillations are significant before the wave event appears. This is observed for 7 of 21 events, where 3 among the 7 events are strongly dominated by the effect.

We observe that slamming plays a dominant role for the largest response events. Apart from one of the preceding wave cases, large nonlinear inertia forces are present for all of the events, where either the front or back of the wave, or both, are observed to be

Event	Series	t [s]	$T_{TT}\sqrt{g/D}$	$k_{TT}\eta_C$	$F_{I,front}$	$F_{I,back}$	F_{slam}	F_{II}	R_{opp}	λ_{prec}
(1)	b	154.8	15.5	0.21	N	Y	Y	Y	Y	Y
(2)	d	250.1	10.7	0.41	Y	Y	Y	Y	Y	N
(3)	c	155.7	10.8	0.38	Y	Y	Y	Y	Y	N
(4)	e	229.6	15.0	0.30	Y	Y	Y	Y	Y	Y
(5)	e	101.8	11.0	0.44	Y	Y	N	Y	Y	N
(6)	c	156.5	12.2	0.21	N	N	N	N	N	Y(S)
(7)	e	118.0	9.8	0.44	Y	Y	N	Y	Y	N
(8)	e	151.3	13.2	0.25	N	Y	Y	Y	Y	N
(9)	d	146.7	11.5	0.24	N	Y	N	Y	Y	N
(10)	e	112.2	11.8	0.35	Y	Y	N	Y	Y	N
(11)	e	265.4	11.8	0.36	Y	Y	Y	Y	Y	N
(12)	e	22.3	12.6	0.28	Y	N	N	Y	N	Y(S)
(13)	e	94.2	12.6	0.32	Y	Y	N	Y	Y	N
(14)	f	274.3	10.8	0.34	N	Y	Y	Y	Y	Y
(15)	f	30.5	10.6	0.37	Y	Y	N	Y	Y	N
(16)	c	265.7	11.7	0.25	Y	N	N	N	N	N
(17)	f	69.3	10.4	0.34	N	Y	N	Y	Y	N
(18)	e	24.0	13.8	0.24	Y	N	N	N	N	Y(S)
(19)	b	105.6	10.8	0.31	Y	Y	Y	Y	Y	Y
(20)	f	128.1	8.8	0.44	Y	Y	N	Y	Y	N
(21)	b	170.0	12.7	0.26	Y	N	N	N	N	N

TABLE 3. Wave parameters and observed wave load and response characteristics, for the 21 largest response events when $\omega_0/\omega_P = 3$, listed in decreasing order with respect to r^{max}/σ_M . The characteristics are confirmed with Y = Yes, N = No or Y(S) = Yes, strongly dominated. Parameters in the table: event number, series index, time of occurrence and the rest of the parameters are defined in the text.

steep. However, the large inertia force and the resulting response rather occurs for a large elevation gradient in the back of the wave while what happens in the wave front is less important. Apart from one preceding wave case, the secondary load cycle is found to coincide with the steep wave gradient in the back of the wave.

3.4. Nonlinear vs. linear exceedance probability

The empirical exceedance probabilities of the nonlinear wave-exciting moment and motion response are found using (2.2). Each of the series are considered separately, where the frequency ratio is varied with $\omega_0/\omega_P = 3, 4$ or 5. The load and responses are presented for increasing nonlinearity ($0.10 < \epsilon_P < 0.14$) and for long and moderately long waves ($0.09 < k_{Pr} < 0.14$).

Estimates for the linear wave-exciting moment and motion response were carried out for reference purposes. In order to estimate the underlying linear wave spectrum, the measured surface elevation was linearised as proposed by Johannessen (2010, 2012). The second order contribution was calculated from the measured wave time series, using the total surface elevation. Subsequently, the linear surface elevation was found by subtracting the second order contribution from the measured surface elevation. Further, irregular waves were created from each of the estimated linear wave spectra. The MacCamy &

Fuchs solution (1954) was used to obtain the wave-exciting moment for a fixed cylinder. More details are found in appendix B.

As expected, the linear and nonlinear analyses agree well for $\omega_0/\omega_P = 3$ when the waves are long and have small amplitude ($\epsilon_P = 0.10$ and $k_{Pr} = 0.09$, figure 8a). The same is true when the wave slope is moderate and the waves are long ($\epsilon_P = 0.12$ and $k_{Pr} = 0.09$, figure 8b). In these cases the estimated linear response provides a good representation of the nonlinear probability.

For moderate wave slope and moderately long waves ($\epsilon_P = 0.12$ and $k_{Pr} = 0.11$, figure 8c) the linear estimate gives a good representation of the distribution of the response for $P_{ex}(R^{max}/\sigma_M) > 0.06$. However, for $P_{ex}(R^{max}/\sigma_M) < 0.06$ the nonlinear contribution becomes significant, showing a deviation of $\sim 50\%$ for the largest nonlinear response events (marked by circles) when compared to the corresponding linear estimate. For steeper and shorter waves, we observe that the deviation appears at an earlier stage: for $\epsilon_P = 0.12$ and $k_{Pr} = 0.14$ $P_{ex}(R^{max}/\sigma_M) \sim 0.1$ (figure 8d), for $\epsilon_P = 0.14$ and $k_{Pr} = 0.09$ $P_{ex}(R^{max}/\sigma_M) \sim 0.2$ (figure 8e) and for $\epsilon_P = 0.14$ and $k_{Pr} = 0.14$ $P_{ex}(R^{max}/\sigma_M) \sim 0.3$ (figure 8f). For the steepest waves ($\epsilon_P = 0.14$) the nonlinear force deviates earlier from the linear force for longer waves (compare figures 8e and 8f). We note that while the wave-exciting moment is dominated by the energy around the governing wave frequency, the response is governed by the nonlinear high frequency forces.

For $\omega_0/\omega_P = 4$ the response for small wave slope and long waves ($\epsilon_P = 0.10$ and $k_{Pr} = 0.09$, figure 9a) follows the linear results, but shows a deviating trend for small exceedance probability. For moderate wave slope and long waves ($\epsilon_P = 0.12$ and $k_{Pr} = 0.09$, figure 9a) the deviation between the nonlinear and linear results becomes evident for $P_{ex} \approx 0.1$. In moderate and steep waves ($\epsilon_P > 0.12$, figures 9b – 9f) a significant deviation between the nonlinear and linear results is found for $P_{ex} < 0.2$. For $\omega_0/\omega_P = 5$ the same tendencies as for $\omega_0/\omega_P = 4$ are observed. When the frequency is increased, the response tends towards the wave-exciting moment, which is equivalent with the quasi-static level.

As expected, the linear and nonlinear analyses agree well when the waves are long and have small amplitude. The nonlinearity of the wave-exciting moment becomes more important in the steeper and shorter waves. The nonlinearity also becomes more prominent when the frequency ratio ω_0/ω_P is increased from 3 to 4.

3.5. Extreme response events

The most extreme responses are critical for design. It is of interest to further investigate the wave effects driving these responses. The 1% largest events (satisfying $P_{ex}(R^{max}/\sigma_M) < 10^{-2}$) are presented in scatter diagrams according to the wave proxies $T_{TT}\sqrt{g/d}$ and $k_{TT}\eta_C$. The resonance frequencies are $\omega_0/\omega_P = 3, 4$ and 5. The majority of these events occur for waves with period $T_{TT}\sqrt{g/d}$ between 9 and 16 and wave slope $k_{TT}\eta_C$ larger than 0.2 (figures 10a, 10c and 10e).

In order to discuss the history effect in the response, i.e the contribution from the inertia of the moving pile due to successive large wave events, we present calculations with a damping of both $\zeta = 0.02$ and $\zeta = 0.06$, where in the latter the effect of preceding waves, for the local response, is smaller compared to the former. The extreme response events obtained with $\zeta = 0.06$ all gather in a common region (figures 10b, 10d and 10f).

The nonlinear high frequency forces driving the response originates either from flow separation, free surface gravity waves, or a combination. Flow separation is governed by the Keulegan-Carpenter number $KC = u_C T_{TT}/d$, while gravity wave effects are governed by the Froude number $Fr = u_C/\sqrt{gd}$. We have in figure 10 indicated the line corresponding to $KC = 5$. Almost all of the extreme events are found for $KC > 5$ and

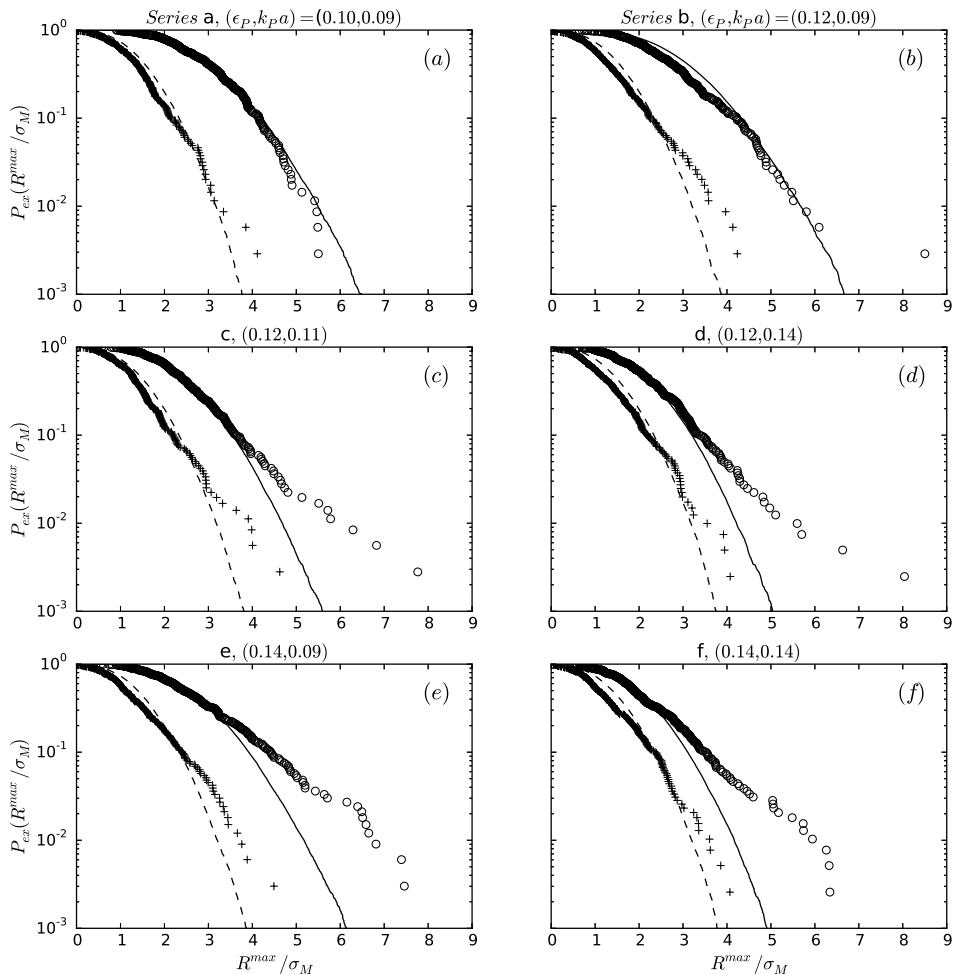


FIGURE 8. The empirical exceedance probability for linear wave-exciting moment (– –), nonlinear wave-exciting moment (+), linear motion response (—) and nonlinear motion response (o) where $\omega_0/\omega_P = 3$ for (a) series a, $(\epsilon_P, k_{Pa}) = (0.10, 0.09)$, (b) b, $(0.12, 0.09)$, (c) c, $(0.12, 0.11)$, (d) d, $(0.12, 0.14)$, (e) e, $(0.14, 0.09)$ and (f) f, $(0.14, 0.14)$,

$k_{TT}\eta_C > 0.15$. Note that a KC -number larger than 2 is commonly associated with flow separation (Sarpkaya 1986).

The contribution of flow separation to the higher harmonic wave forces has recently been suggested by Paulsen *et al.* (2014b); Kristiansen & Faltinsen (2017). We remark that the details of the flow separation depends on the Reynolds number (Re) and are different in the model scale compared to the large scale, where Re is approximately 1000 times larger. The possible flow separation may contain more three dimensional effects in the large scale compared to the model scale.

We have also indicated the line $Fr = 0.4$, where $Fr = u_C/\sqrt{gd}$. The extreme response

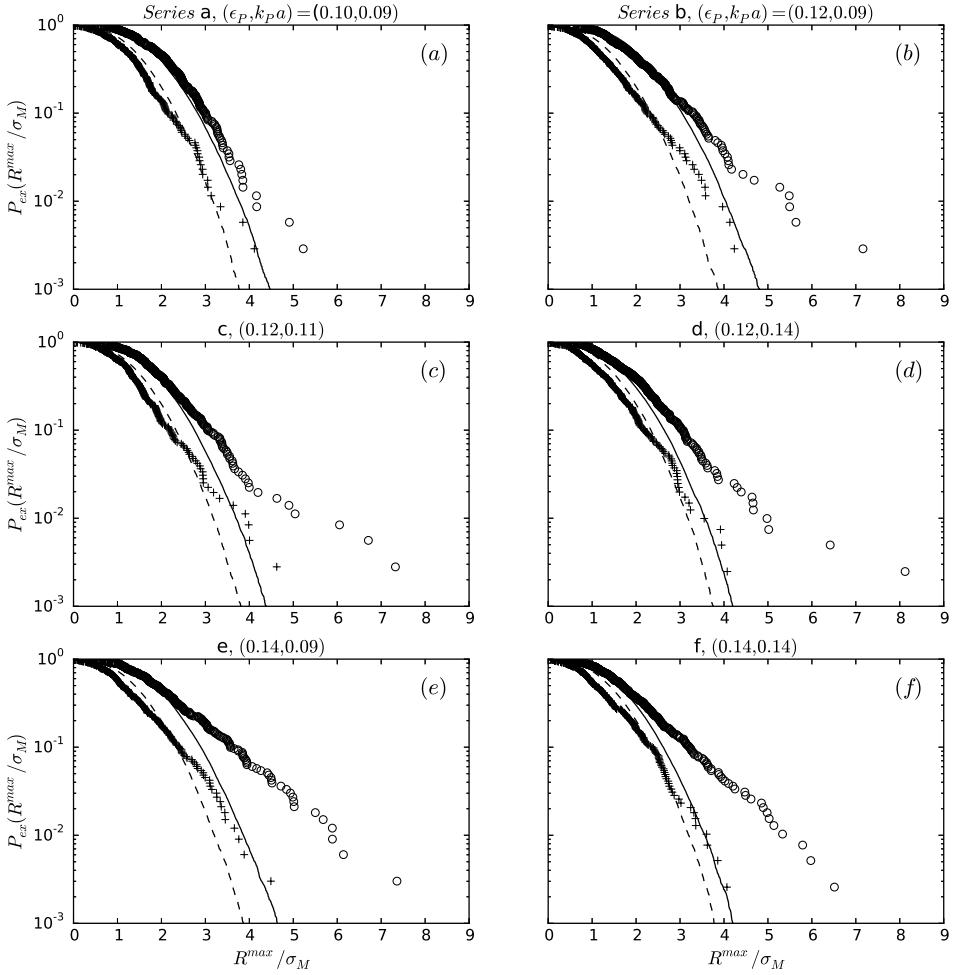


FIGURE 9. The empirical exceedance probability for linear wave-exciting moment (—), nonlinear wave-exciting moment (+), linear motion response (—) and nonlinear motion response (o) where $\omega_0/\omega_P = 4$ for (a) series a, $(\epsilon_P, k_P a) = (0.10, 0.09)$, (b) b, $(0.12, 0.09)$, (c) c, $(0.12, 0.11)$, (d) d, $(0.12, 0.14)$, (e) e, $(0.14, 0.09)$ and (f) f, $(0.14, 0.14)$,

events found for waves with $Fr < 0.4$ are all affected by preceding waves. The Froude number indicates a gravity wave effect at the scale of the cylinder diameter, where $Fr = 0.4$ corresponds to a local wavelength $\lambda_C = 2\pi u_C^2/g$ of the local crest velocity u_C with $\lambda_C \approx d$ contributing to a particular wave-body interaction, as proposed by Grue *et al.* (1993, 1994).

The present data of the obtained responses show that the extreme events occur for $KC > 5$. The regime $KC > 5$, is significantly above the separation limit ($KC > 2$, Sarpkaya 1986), indicating a flow separation effect and contribution from possible drag forces, even though the flow separation itself has not been measured. The findings

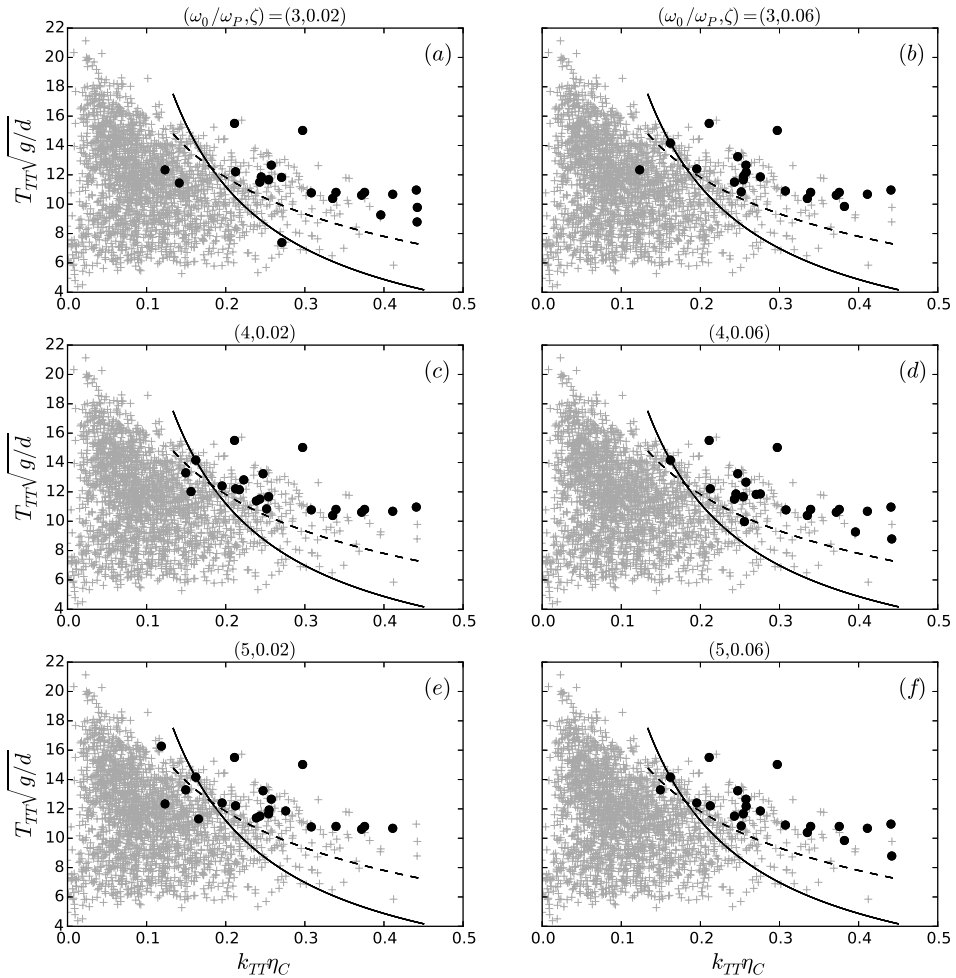


FIGURE 10. Wave scatter plot including all the 2166 events (+), events with $P_{ex}(R^{max}/\sigma_M) < 0.01$ (\bullet), $Fr = 0.4$ (—) and $KC = 5$ (---) for (a) $(\omega_0/\omega_P, \zeta) = (3, 0.02)$, (b) $(3, 0.06)$, (c) $(4, 0.02)$, (d) $(4, 0.06)$, (e) $(5, 0.02)$ and (f) $(5, 0.06)$.

supports KC and flow separation as a more relevant criterion for the extreme response events. However, we choose to include the Froude criterion, as the results are not considered sufficient in order to exclude the surface gravity wave effects. The more visible local free surface wave, suggested at the cylinder diameter scale, is for comparison governed by $Fr > 0.4$. The free surface effect is very clear in the experiments. The wave may co-interact with the flow separation effects, suggesting that both effects and criteria are relevant.

4. Conclusions

The high frequency resonant responses of a weakly damped monopile exposed to irregular deep water waves have been investigated. The response events were obtained accounting for the short term wave statistics. Experiments were carried out with a single bottom hinged cylinder in two different set-ups. In the first set-up the cylinder was fixed, while in the other it was free to oscillate, obtaining both the wave-exciting moment and the motion response. The nonlinearity, peak wave number and peak period of the six different wave series were in the ranges: $\epsilon_p \sim 0.10 - 0.14$, $k_{Pr} \sim 0.09 - 0.14$ and $T_P\sqrt{g/d} \sim 12.0 - 14.8$, respectively, where all quantities are defined in §2.2.

By use of a transfer function, the response was calculated from the measured wave-exciting moment on the fixed cylinder. The calculations of the extreme response maxima compares very well with the measured ones. The accuracy is approximately 5%. The overall agreement is even better when comparing the sorted maxima (the so-called quantiles). This justifies the use of the measured wave-exciting moment in combination with the transfer function, both for estimating the probability distributions and for calculating the response level of the extreme events. The response is then discussed as function of the resonance frequency ω_0 , which is varied in the range where $\omega_0/\omega_P \sim 3 - 5$.

The empirical short term exceedance probability distributions of the nonlinear wave-exciting moment and motion response, obtained for each of the six series, show: for small wave slope ($\epsilon_P = 0.10$), long waves ($k_{Pr} = 0.09$) and a resonance frequency of $\omega_0/\omega_P = 3$, the nonlinear response analyses agree, and is in fact very well represented by its linear counterpart. The same is true for a moderate wave slope ($\epsilon_P = 0.12$) and long waves ($k_{Pr} = 0.09$). By increasing the ratio ω_0/ω_P to 4 or 5, the importance of the nonlinearities becomes apparent, where the deviation between the nonlinear and linear calculations occurs for an exceedance probability of $P_{ex}(R^{max}/\sigma_M) < 0.1$. For moderate to strong waves ($\epsilon_P \sim 0.12 - 0.14$) and long to moderately long waves ($k_{Pr} \sim 0.09 - 0.14$), the deviation between the nonlinear and linear results are clear in all cases. The deviation starts earlier for $\omega_0/\omega_P = 4, 5$ compared to $\omega_0/\omega_P = 3$, as well as for an increasing wave slope, and for a decreasing wavelength.

The most extreme response events, moreover are obtained according to the local wave proxies: the local trough-to-trough period $T_{TT}\sqrt{g/d}$ and the local wave slope estimate $k_{TT}\eta_C$. The events are found in a region where the Keulegan-Carpenter number exceeds $KC > 5$, indicating that possible flow separation effects contribute to the extreme responses. The contribution of flow separation to the higher harmonic wave forces has been recently suggested by Paulsen *et al.* (2014b); Kristiansen & Faltinsen (2017). A similar region is also covered by a Froude number exceeding $Fr > 0.4$ pointing to surface gravity wave effects at the scale of the cylinder diameter as suggested by Grue *et al.* (1993, 1994). It is still an open research question if either of the effects are dominating or of equal importance.

From a number of large response events, different wave load mechanisms are discussed: i) wave-exciting inertia forces, a function of the fluid acceleration; ii) wave slamming due to both non-breaking and breaking wave events; iii) the secondary load cycle; and iv) possible drag forces, a function of the fluid velocity.

The 3rd, 4th and 5th harmonic wave-exciting force components are extracted by their ensemble average and standard deviation in the irregular waves. They are expressed by the local wave proxies. The present results, for a wave slope up to 0.3, fit well to and generalize the results in regular waves for a wave slope up to 0.24 of Huseby & Grue (2000). The 3rd harmonic force in the longer waves shows good agreement with the FNV-method.

The JONSWAP spectrum was chosen to approximate real ocean environment. In general, the findings are expected to apply for a broader range of storm conditions, i.e. other spectral shapes. However, one should be careful when there are possibilities for linear induced high frequency response, such as in combined wind and swell sea, i.e. two peak spectra.

The study has been carried out with financial support from Stiftelsen Det Norske Veritas, DNV GL and The Research Council of Norway. The technical assistance during the experimental work by Head Engineer Olav Gundersen is gratefully acknowledged.

Appendix A

The vertical cylinder may rotate with an angle $\theta(t)$ in the pitch mode of motion about a hinge at the bottom, located at $z = z_0 = 2$ cm above the tank floor. Assuming linear motion, the moment due to the pressure forces with respect to z_0 reads: $M_{wave}(t) - a_{55}\ddot{\theta} - b_{55}\dot{\theta} - c_{55}\theta$, where $M_{wave}(t)$, a_{55} , b_{55} and c_{55} denote the wave exciting moment, added mass, damping and restoring coefficients in the pitch mode of motion, respectively. The moment due to the spring forces reads: $-(z_a - z_0)(F_2(t) - F_1(t)) = -\kappa_0(z_a - z_0)^2\theta$ where z_a denotes the height of the force transducers, $F_1(t)$ and $F_2(t)$ denote the force recorded on the left and right transducer, respectively, see figure 4, and κ_0 the spring constant. Balance of angular momentum gives

$$m_{55}\ddot{\theta} = -a_{55}\ddot{\theta} - b_{55}\dot{\theta} - (\kappa_0(z_a - z_0)^2 + c_{55})\theta + M_{wave}(t), \quad (\text{A } 1)$$

where m_{55} denotes the moment of inertia of the water filled cylinder. This obtains

$$\ddot{\theta} + 2\zeta\omega_0\dot{\theta} + \omega_0^2\theta = M_{wave}(t)/(m_{55} + a_{55}), \quad (\text{A } 2)$$

where the resonance frequency is given by $\omega_0^2 = (c_{55} + \kappa_0(z_a - z_0)^2)/(m_{55} + a_{55})$. Note that the spring force provides the dominant contribution to the restoring force where c_{55} is 0.005 times $\kappa_0(z_a - z_0)^2$ for the actual cylinder. The still water decay tests as well as the irregular wave experiments determine $\omega_0 = 17.7$ rad/s of the oscillating cylinder. The damping ratio ζ , determined as the fraction of the critical damping, is 0.02 for the cylinder. In the experiments with the fixed cylinder set-up, small vibrations are measured at frequencies $\omega > 88$ rad/s. These are driven by the wave maker and transferred through the tank frame to the cylinder set-up.

Eq. (A 2) may be expressed on matrix form: $(d/dt)(e^{At}Y) = e^{At}[0, M_{wave}(t)]/((m_{55} + a_{55})\omega_\zeta)^T$ where $Y = [\theta, y]^T$, $[\]^T$ denotes the transpose, $\theta + \zeta\omega_0\theta = \omega_\zeta y$, and $\omega_\zeta = \omega_0\sqrt{1 - \zeta^2}$. The matrix A and its variant e^{At} are expressed by

$$A = \begin{pmatrix} \zeta\omega_0 & -\omega_\zeta \\ \omega_\zeta & \zeta\omega_0 \end{pmatrix}, \quad e^{At} = e^{\zeta\omega_0 t} \begin{pmatrix} \cos \omega_\zeta t & -\sin \omega_\zeta t \\ \sin \omega_\zeta t & \cos \omega_\zeta t \end{pmatrix}. \quad (\text{A } 3)$$

By integration, the pitch angle $\theta(t)$ is obtained as function of time. For convenience this is multiplied by $\kappa_0(z_a - z_0)^2$ obtaining the moment of the sum spring force with respect to z_0 . We denote this quantity by $R(\omega_0, t)$ where

$$R(\omega_0, t) = \kappa_0(z_a - z_0)^2\theta(t) = \frac{\omega_0^2}{\omega_\zeta} \int_0^t M_{wave}(\tau)e^{-\zeta\omega_0(t-\tau)} \sin(\omega_\zeta(t - \tau))d\tau. \quad (\text{A } 4)$$

Appendix B

In order to estimate the underlying linear wave spectrum the measured surface elevation, η , is linearised as proposed by Johannessen (2010, 2012). The second order contribution, $\eta^{(2)}$, is calculated using finite depth theory (Sharma & Dean 1981), where only nearby wave components are allowed to interact. This is implemented by a maximum bandwidth between the interacting wave components $\delta\omega = 0.8\omega_P$. The prime denotes the use of the total surface elevation for the calculations of the second order contribution. Then the resulting linear surface elevation, $\eta^{(1)}$, is found by

$$\eta - \eta^{(2)} = (\eta^{(1)} + \eta^{(2)} + \dots) - (\eta^{(2)} + O^{(3)}) = \eta^{(1)} + O^{(3)} \quad (\text{B1})$$

being accurate to and including second order effects. Subsequently, theoretical realizations of irregular waves were created from each of the linear wave spectra, with random phase. The MacCamy & Fuchs solution (1954) was used to obtain the linear wave-exciting moment for a fixed cylinder. The standard deviation of the linear part is, on average for the six series, 1% smaller than the measured and fully nonlinear wave-exciting moment. Finally, the response transfer function (A 4) was used to calculate the linear motion response.

REFERENCES

- BREDMOSE, H., SLABIAK, P., SAHLBERG-NIELSEN, L. & SCHLÜTTER, F. 2013 Dynamic excitation of monopiles by steep and breaking waves. experimental and numerical study. In *Proceedings of the ASME 2013 32nd International Conference on Ocean, Offshore and Arctic Engineering*.
- CHAPLIN, J. R., RAINEY, R. C. T. & YEMM, R. W. 1997 Ringing of a vertical cylinder in waves. *Journal of Fluid Mechanics* **350**, 119–147.
- FALTINSEN, O. M. 1993 *Sea loads on ships and offshore structures*. Cambridge university press.
- FALTINSEN, O. M., NEWMAN, J. N. & VINJE, T. 1995 Nonlinear wave loads on a slender vertical cylinder. *Journal of Fluid Mechanics* **289**, 179–198.
- FORRISTALL, G. Z. 2000 Wave crest distributions: Observations and second-order theory. *Journal of physical oceanography* **30** (8), 1931–1943.
- GODA, Y. & SUZUKI, Y. 1976 Estimation of incident and reflected waves in random wave experiments. In *Coastal Engineering 1976*, pp. 828–845. American Society of Civil Engineers.
- GRUE, J., BJØRSHOL, G. & STRAND, Ø. 1993 Higher harmonic wave exciting forces on a vertical cylinder. In *Preprint series. Mechanics and Applied Mathematics, available on <http://urn.nb.no/URN:NBN:no-52740>*, pp. 1–30. University of Oslo.
- GRUE, J., BJØRSHOL, G. & STRAND, Ø. 1994 Nonlinear wave loads which may generate 'ringing' responses of offshore structures. In *Ninth International Workshop on Water Waves and Floating Bodies, available on www.fb.org*. (ed. M. Ohkusu), pp. 77–81.
- GRUE, J., CLAMOND, D., HUSEBY, M. & JENSEN, A. 2003 Kinematics of extreme waves in deep water. *Applied Ocean Research* **25** (6), 355–366.
- GRUE, J. & HUSEBY, M. 2002 Higher-harmonic wave forces and ringing of vertical cylinders. *Applied ocean research* **24** (4), 203–214.
- GRUE, J. & JENSEN, A. 2012 Orbital velocity and breaking in steep random gravity waves. *Journal of Geophysical Research: Oceans* **117** (C7).
- HASSELMANN, K., BARNETT, T. P., BOUWS, E., CARLSON, H., CARTWRIGHT, D. E., ENKE, K., EWING, J. A., GIENAPP, H., HASSELMANN, D. E., KRUSEMAN, P., MEERBURG, A., MÜLLER, P., OLBERS, D. J., RICHTER, K., SELL, W. & WALDEN, H. 1973 Measurements of wind-wave growth and swell decay during the joint north sea wave project (jonswap). *Tech. Rep.*. Deutsches Hydrographisches Institut.
- HAYER, S. & WINTERSTEIN, S. R. 2009 Environmental contour lines: A method for estimating long term extremes by a short term analysis. *Transactions of the Society of Naval Architects and Marine Engineers* **116**, 116–127.

- HUSEBY, M. & GRUE, J. 2000 An experimental investigation of higher-harmonic wave forces on a vertical cylinder. *Journal of Fluid Mechanics* **414**, 75–103.
- JOHANNESSEN, T. B. 2010 Calculations of kinematics underneath measured time histories of steep water waves. *Applied Ocean Research* **32** (4), 391–403.
- JOHANNESSEN, T. B. 2012 Nonlinear superposition methods applied to continuous ocean wave spectra. *Journal of Offshore Mechanics and Arctic Engineering* **134** (1), 011302.
- KALLEHAVE, D., BYRNE, B. W., THILSTED, C. L. & MIKKELSEN, K. K. 2015 Optimization of monopiles for offshore wind turbines. *Phil. Trans. R. Soc. A* **373** (2035), 20140100.
- KRISTIANSEN, T. & FALTINSEN, O. M. 2017 Higher harmonic wave loads on a vertical cylinder in finite water depth. *Journal of Fluid Mechanics* **833**, 773–805.
- KROKSTAD, J. R., STANSBERG, C. T., NESTEGÅRD, A. & MARTHINSEN, T. 1998 A new non-slender ringing load approach verified against experiments. *Journal of Offshore Mechanics and Arctic Engineering* **120** (1), 20–29.
- LIGHTHILL, J. 1979 Waves and hydrodynamic loading. In *Proceedings of the Second International Conference on Behaviour of Off-Shore Structures (BOSS)*, pp. 1–40. BHRA Fluid Engineering.
- LIGHTHILL, J. 1986 Fundamentals concerning wave loading on offshore structures. *Journal of Fluid Mechanics* **173**, 667–681.
- MALENICA, Š. & MOLIN, B. 1995 Third-harmonic wave diffraction by a vertical cylinder. *Journal of Fluid Mechanics* **302**, 203–229.
- MARTHINSEN, T., STANSBERG, C. T. & KROKSTAD, J. R. 1996 On the ringing excitation of circular cylinders. In *The Sixth International Offshore and Polar Engineering Conference*, pp. 196–204. International Society of Offshore and Polar Engineers.
- MORISON, J. R., O'BRIEN, M. P., JOHNSON, J. W. & SCHAAF, S. A. 1950 The force exerted by surface waves on piles. *Journal of Petroleum Technology* **2** (05), 149–154.
- NEWMAN, J. N. 1996 Nonlinear scattering of long waves by a vertical cylinder. In *Waves and nonlinear processes in hydrodynamics* (ed. J. Grue, B. Gjevik & J. E. Weber), pp. 91–102. Springer.
- PAULSEN, B. T., BREDMOSE, H. & BINGHAM, H. B. 2014a An efficient domain decomposition strategy for wave loads on surface piercing circular cylinders. *Coastal Engineering* **86**, 57–76.
- PAULSEN, B. T., BREDMOSE, H., BINGHAM, H. B. & JACOBSEN, N. G. 2014b Forcing of a bottom-mounted circular cylinder by steep regular water waves at finite depth. *Journal of Fluid Mechanics* **755**, 1–34.
- RAINEY, R. C. T. 1989 A new equation for calculating wave loads on offshore structures. *Journal of Fluid Mechanics* **204**, 295–324.
- RAINEY, R. C. T. 1995a The hydrodynamic load at the intersection of a cylinder with the water surface. In *Proceedings of 10th International Workshop on Water Waves and Floating Bodies* (ed. R. Eatock Taylor), pp. 207–210.
- RAINEY, R. C. T. 1995b Slender-body expressions for the wave load on offshore structures. In *Proceedings of the Royal Society of London A: Mathematical, Physical and Engineering Sciences, vol. 450*, pp. 391–416. The Royal Society.
- SARPKAYA, T. 1986 Force on a circular cylinder in viscous oscillatory flow at low keulegancarpenter numbers. *Journal of Fluid Mechanics* **165**, 61–71.
- SCHLØER, S., BREDMOSE, H. & BINGHAM, H. B. 2016 The influence of fully nonlinear wave forces on aero-hydro-elastic calculations of monopile wind turbines. *Marine Structures* **50**, 162–188.
- SHARMA, J. N. & DEAN, R.G. 1981 Second-order directional seas and associated wave forces. *Society of Petroleum Engineers Journal* **21** (01), 129–140.
- STANSBERG, C. T. 1997 Comparing ringing loads from experiments with cylinders of different diameters – an empirical study. In *The Eighth Conference on the Behaviour of Offshore Structures (BOSS '97), vol. 2*, pp. 95–109. Pergamon/Elsevier.
- STANSBERG, C. T., GUDMESTAD, O. T. & HAVER, S. K. 2008 Kinematics under extreme waves. *Journal of Offshore Mechanics and Arctic Engineering* **130** (2), 021010.
- STANSBERG, C. T., HUSE, E., KROKSTAD, J. R. & LEHN, E. 1995 Experimental study of non-linear loads on vertical cylinders in steep random waves. In *The Fifth International*

- Offshore and Polar Engineering Conference*, pp. 75–82. International Society of Offshore and Polar Engineers.
- TROMANS, P., SWAN, C. & MASTERTON, S. 2006 Nonlinear potential flow forcing: the ringing of concrete gravity based structures. *Tech. Rep.* HSE Report 468. Health and Safety Executive, United Kingdom.
- TROMANS, P. S., ANATURK, A. R. & HAGEMEIJER, P. 1991 A new model for the kinematics of large ocean waves-application as a design wave. In *The First International Offshore and Polar Engineering Conference*. International Society of Offshore and Polar Engineers.
- WHEELER, J. D. 1970 Methods for calculating forces produced by irregular waves. *Journal of Petroleum Technology* pp. 359–367.
- ZHEN, G., BINGHAM, H. B., NICHOLLS-LEE, R. & OTHERS 2015 Offshore renewable energy. In *19th International Ship and Offshore Structures Congress*.